

Complex supramolecular interfacial tessellation through convergent multi-step reaction of a dissymmetric simple organic precursor

Yi-Qi Zhang^{1*}, Mateusz Paszkiewicz¹, Ping Du², Liding Zhang¹, Tao Lin¹, Zhi Chen², Svetlana Klyatskaya², Mario Ruben^{2,3*}, Ari P. Seitsonen⁴, Johannes V. Barth^{1*} and Florian Klappenberger^{1*}

Interfacial supramolecular self-assembly represents a powerful tool for constructing regular and quasicrystalline materials. In particular, complex two-dimensional molecular tessellations, such as semi-regular Archimedean tilings with regular polygons, promise unique properties related to their nontrivial structures. However, their formation is challenging, because current methods are largely limited to the direct assembly of precursors, that is, where structure formation relies on molecular interactions without using chemical transformations. Here, we have chosen ethynyl-iodophenanthrene (which features dissymmetry in both geometry and reactivity) as a single starting precursor to generate the rare semi-regular (3.4.6.4) Archimedean tiling with long-range order on an atomically flat substrate through a multi-step reaction. Intriguingly, the individual chemical transformations converge to form a symmetric alkynyl-Ag-alkynyl complex as the new tecton in high yields. Using a combination of microscopy and X-ray spectroscopy tools, as well as computational modelling, we show that *in situ* generated catalytic Ag complexes mediate the tecton conversion.

Supramolecular chemistry^{1,2} provides fascinating routes to synthesize versatile architectures by making use of fundamental spontaneous ordering principles. Semi-regular Archimedean tilings (ATs)^{3,4} and quasicrystalline structures (QCs)^{5,6} are of particular interest, because materials based on such structures possess intriguing physical^{7–9} and chemical properties¹⁰. Recent progress in this regard has been achieved in various fields, including the programmed self-assembly of DNA molecules^{11,12}, liquid-crystal engineering¹³, binary nanoparticle superlattices¹⁴ and polymeric systems^{15,16}. In the past decade, interfacial supramolecular engineering^{17–20}, where molecular tectons form architectures through specific interactions between functional groups²¹ or metal-directed assembly²⁰, has enabled the synthesis of two-dimensional semi-regular ATs^{22–25} and QCs^{26,27}. Moreover, the employment of molecular tectons with reduced symmetries²⁸ has shown great potential to form complex two-dimensional supramolecular arrangements, expressing random glasses^{29,30}, fractal patterns^{31,32} or other complex tilings^{33–35}. However, this approach has so far been limited generally to directly accessible constructs, that is, where structure formation relies only on the interactions between the primary constituents, and not on their multiple chemical transformations.

Here, we introduce a methodology implementing multi-step convergent synthesis (Fig. 1). Our findings demonstrate how chemical conversions of a simple organic species afford previously inaccessible architectures. We utilize a bifunctional molecular tecton, ethynyl-iodophenanthrene (EIP, **1**), which features dissymmetry in the geometry of its backbone (phenanthrene) and in the reactivity of its functional groups (an H-terminated alkynyl group in the 2 position and an iodine substitution in the 7 position; Fig. 1, upper left). Following thermal annealing on Ag(111), a striking transformation from a

simple regular (6³) network assembled at low annealing temperature ($T_{\text{ann}} \leq 130$ K) to a well-ordered semiregular (3.4.6.4) tiling ($300 \text{ K} \leq T_{\text{ann}} \leq 350$ K) is observed. These two types of regular architecture are separated by a disordered stage in the temperature range $130 < T < 300$ K, where multiple on-surface reactions proceed simultaneously and generate various intermediate species, which eventually afford the essential building block underlying expression of the spontaneously assembled (3.4.6.4) AT (Fig. 1, right). Complementary scanning tunnelling microscopy (STM), X-ray spectroscopy (XS)²¹ and density functional theory (DFT) investigations reveal the chemical nature of the molecular ATs and elucidate the convergent reaction pathway, including a H transfer from the terminal alkyne to the dehalogenated site on the phenanthrene backbone mediated by *in situ* generated catalytic Ag complexes at low temperature. Overall, these results demonstrate a novel approach towards achieving materials with increased structural complexity³⁶.

Results and discussion

Fabrication of ATs. After depositing EIP (**1**) molecules onto a cold Ag(111) substrate, intact EIP (**1**) molecules self-assembled into a porous network on the flat surface, expressing a simple and regular (6³) AT (Fig. 2a). Structural analysis (Supplementary Fig. 1), supported by DFT calculations, shows that the bonding motifs in this network feature a three-fold chiral organization for both the terminal alkynes and the iodine groups, implying weak C–H... π interaction³⁷ and halogen bonding^{38,39}, respectively (blue and red dashed circles in Fig. 2a,b).

In an annealing temperature range between 200 and 250 K, irregular arrangements evolve (Fig. 2c,d); the chemical nature of which is discussed in the following. Moreover, after annealing the sample to

¹Physik-Department E20, Technische Universität München, 85748 Garching, Germany. ²Institute of Nanotechnology, Karlsruhe Institute of Technology, 76344 Eggenstein-Leopoldshafen, Germany. ³IPCMS-CNRS, Université de Strasbourg, 23 rue de Loess, 67034 Strasbourg, France. ⁴École Normale Supérieure, Département de Chimie, 24 rue Lhomond, F-75005 Paris, France.

*e-mail: yiqi.zhang@tum.de; mario.ruben@kit.edu; jvb@tum.de; florian.klappenberger@tum.de

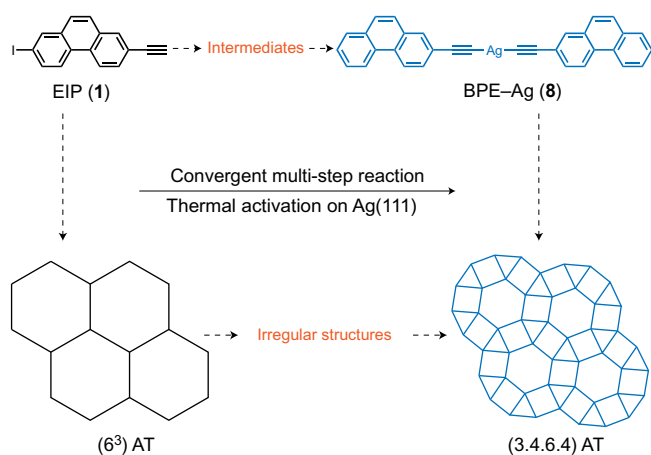


Figure 1 | Supramolecular (3.4.6.4) AT formation through interfacial chemical conversion of primary tectons by a convergent reaction scheme.

Intact ethynyl-iodophenanthrene (EIP, **1**) molecules form supramolecular (6^3) AT on Ag(111) at $T_{\text{ann}} \leq 130$ K. Following a multi-step convergent reaction pathway, a complex supramolecular (3.4.6.4) AT forms at $T_{\text{ann}} = 300\text{--}350$ K with a newly generated building block, bis(phenanthren-2-ylethynyl)silver (BPE-Ag, **8**), which is the major outcome ($\sim 92\%$) of the convergent reaction. In the temperature range 130 K $< T_{\text{ann}} < 300$ K, the various intermediates generated through on-surface reactions form irregular structures.

$300\text{--}350$ K, a striking transformation to an ordered complex architecture was observed (Fig. 2e,f). The novel phase is constructed from interwoven 12-segmented rings (highlighted in yellow), creating pores that host further species. The crystalline network exhibits long-range order in the 100 nm range (Supplementary Fig. 2). The crossings of the interwoven rings (red circles in Fig. 3a) represent the four-fold vertices of the architecture consisting of three types of polygon: triangles, tetragons and hexagons. The packing geometry of these three polygons is closely related to one of the eleven ATs: the (3.4.6.4) semi-regular tiling. The respective unit cell is commensurate to the underlying substrate (Fig. 3a) and can be expressed in the matrix representation as:

$$\begin{pmatrix} \mathbf{a} \\ \mathbf{b} \end{pmatrix} = \begin{pmatrix} 10 & -6 \\ 6 & 16 \end{pmatrix} \begin{pmatrix} \mathbf{u} \\ \mathbf{v} \end{pmatrix}$$

where \mathbf{a} and \mathbf{b} are the primitive vectors of the superstructure and \mathbf{u} and \mathbf{v} are the primitive vectors of the Ag(111) substrate. Further analysis shows that the tetragon in the (3.4.6.4) AT is, in fact, a parallelogram with different lengths for its two adjacent edges: $c = 2\sqrt{7}a_0 \approx 15.3$ Å and $d = 2\sqrt{19/3}a_0 \approx 14.5$ Å. The interior angles of the parallelogram can be determined from the epitaxy model as 85.69° and 94.31° (Fig. 3b), respectively.

To unravel the chemical nature of the architecture, we started with a molecular model fitting of the four-fold vertex binding motif (Fig. 3c and Supplementary Fig. 3). Superposing the models of a bis(phenanthren-2-ylethynyl)silver (BPE-Ag, **8**) organometallic complex onto all crossings of the tiling (Fig. 3c) revealed that it represents the essential and only building block of the tessellation and that the second axis of the four-fold bonding motif corresponds to an alkynyl-Ag-alkynyl bridge interacting with the nearby phenanthrene backbones (yellow dashed circle in Fig. 3c). A distance analysis (Supplementary Fig. 4) indicated the presence of non-covalent interactions between the C-H moieties and the electron-rich transition metal^{40–42} as well as the alkynyl π -systems⁴³. The resulting attraction causes a slight geometrical bending of BPE-Ag (**8**) (Supplementary Fig. 5), where six BPE-Ag (**8**) molecules

follow a ring-shaped circle, as presented in Figs 2e and 3c,d. The isolated adatoms, which are trapped in a disorderly manner in the pores, have two different apparent heights (yellow and green arrows in Fig. 3c), implying two different species, which were identified as isolated Ag and I adatoms (Supplementary Fig. 6 and discussion in the following). Interestingly, close inspection of Fig. 3c reveals that both *cis* (red dashed outline) and *trans* (blue dashed outline) conformers of the organometallic building block are present within one domain, without showing any ordering systematics. These conformers are achiral and chiral motifs induced by the surface confinement, and analysis of their adsorption configurations (Supplementary Fig. 7) suggests that both geometries have similar energetics. However, the chiral expression of the domain is related to the organizational chirality⁴⁴ (Supplementary Fig. 5) and is independent of the local chirality of its tectons.

To address the stability of the (3.4.6.4) AT and confirm the nature of the bonding motif, extensive DFT calculations (see Methods) were performed. For simplicity, it was assumed that BPE-Ag (**8**) exhibits the *cis* conformation only (red dashed outline in Fig. 3d) and the hosted guest species (Ag and I atoms) were neglected. The energetically preferred structure depicted in Fig. 3d nicely reproduces the suggested complex molecular arrangement featuring the four-fold bonding motif, and the slight bending of the BPE-Ag unit (**8**).

Chemical transformations driving complex tessellation. As the chemical structure of the tessellation building blocks (BPE-Ag, **8**) differs significantly from the starting EIP molecule (**1**), on-surface reactions must have been triggered upon heating. In the following, based on a complementary STM and XS investigation of samples through stepwise annealing treatment (from 130 to 325 K), we elucidate the intricate nature of the chemical reactions involved.

A sample with submonolayer coverage was prepared at a substrate temperature below 130 K for X-ray photoelectron spectroscopy (XPS) measurements. The C 1s spectrum of this sample displays a dominant peak at 285 eV (Fig. 4a) originating from the convolution of several different carbon species with similar binding energies. The I 3d spectrum shows two well-defined single peaks for I $3d_{5/2}$ and I $3d_{3/2}$ at 621 and 633 eV (Fig. 4b), respectively, indicating that the iodine is chemically bonded to carbon⁴⁵, so the EIP molecules (**1**) remain intact during evaporation and adsorption. The XPS data are consistent with the STM observation that in the open porous phase, terminal alkynes and iodine groups are responsible for the C-H \cdots π and halogen bonding, respectively (Fig. 5a and Supplementary Fig. 8).

On annealing the sample to 200 K, thermal dissociation of the I atom from the phenanthrene backbone is clearly visible in the XPS spectra (Fig. 4b). Two additional new peaks appear at 619 eV for I $3d_{5/2}$ and 631 eV for I $3d_{3/2}$, characteristic of adsorbed atomic iodine⁴⁵. Furthermore, in the C 1s spectra, a shoulder-like feature with a 6% contribution to the total area (blue and violet curves in Fig. 4a) emerged at the low-binding energy side, which was absent before annealing. Similar spectroscopic features were reported earlier, implying C-Ag organometallic bond formations^{46–48}.

STM data taken from a sample (with submonolayer coverage prepared at $T_{\text{sub}} = 96$ K) after 200 K annealing showed that densely packed (DP) molecular islands had formed (Fig. 5b and Supplementary Fig. 9). A closer examination of the DP domain shows that it is composed of intact EIP molecules (**1**), dehalogenated molecules (**2**) and abstracted I atoms (Fig. 5b and Supplementary Fig. 9). The XPS indication of C-Ag bond formation was further confirmed by STM imaging of hybrid Ag complexes—that is, featuring the C-Ag-C bridge—on the open surface (Fig. 5d,e and Supplementary Fig. 9). High-resolution STM imaging combined with DFT modelling provided further insight into the chemical nature of the Ag-organic complexes, where two types evolve after annealing to 200 K. One features a linear backbone with a symmetric

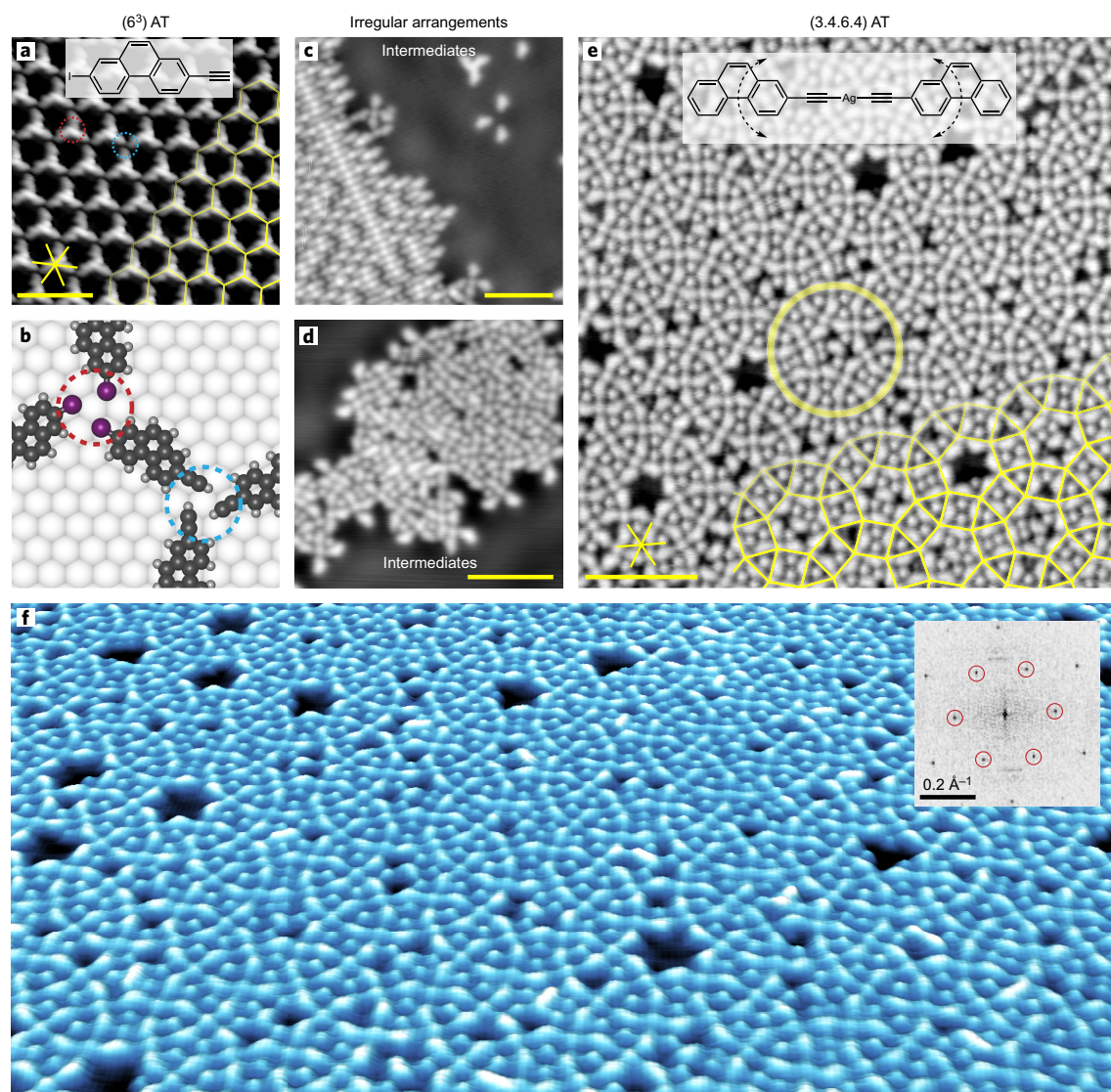


Figure 2 | STM overview of two different AT phases and irregular molecular arrangements on Ag(111). **a**, Hydrogen-bonded and halogen-bonded phase, expressing (6^3) AT as its simplest form, highlighted with a yellow grid (tunnelling current: $I_t = 0.05$ nA, bias voltage: $U_b = 0.2$ V). Inset: Chemical structure of EIP molecule **1**. **b**, DFT-calculated hydrogen-bonded (blue dashed circle) and halogen-bonded (red dashed circle) network of EIP molecules. I, purple; C, grey; H, white. **c,d**, Irregular arrangements of intermediate molecular species generated at $T_{\text{ann}} = 200$ K (**c**) and 250 K (**d**) ($I_t = 0.02$ – 0.2 nA, $U_b = -0.05$ V). **e**, STM overview image of $(3.4.6.4)$ AT, highlighted with the yellow grid. The yellow circle emphasizes the interwoven ring-like structure. $I_t = 0.05$ nA, $U_b = 0.05$ V. Inset: Chemical structure of the BPE-Ag (**8**) building block, with dashed arrows indicating its geometrical flexibility. **f**, Three-dimensional rendering of $(3.4.6.4)$ AT. $I_t = 0.05$ nA, $U_b = 0.05$ V. Inset: Two-dimensional fast Fourier transform of an extended domain shown in Supplementary Fig. 2. In-plane high symmetry directions of the substrates are indicated. Scale bars in all STM images: 50 Å.

aryl–Ag–aryl connection (**4** in Fig. 5d and Supplementary Fig. 9). The distance between the two marked protrusions related to the central arene ring in the phenanthrene backbone is ~ 12 Å (Fig. 5d). The other is characterized by an asymmetric alkynyl–Ag–aryl connection (**6** in Fig. 5e and Supplementary Fig. 9). Notably, one side (alkynyl–Ag) of the bridge has a much narrower width than that of the other (aryl–Ag), and the distance between two protrusions increases to ~ 14 Å. Furthermore, the bridging ethynyl group attracts by C–H $\cdots\pi$ interactions the terminal alkyne groups of two nearby molecules identified as ethynyl-phenanthrene (EP, **3** in Fig. 5e), according to their appearances, as explained in the following. On the open surface, clusters with a three-fold bonding motif replicating the C–H $\cdots\pi$ nodes of the (6^3) network were observed (Fig. 5c and Supplementary Fig. 9). The absence of depressions around the dehalogenated sites⁴³ (Supplementary Fig. 9) indicates that the radical site of the phenanthrene backbone created by I

abstraction was neutralized. We attribute this species to EP (**3**) and explain its formation by hydrogenation through uptake of an atomic H from the surface, because small concentrations of atomic H are typically present under ultrahigh vacuum (UHV) conditions on Ag(111) below 200 K^{49,50}.

After annealing the sample to 325 K, the transition of the peaks in the I 3d XPS spectra towards the low binding energy features at 619 and 631 eV is completed (Fig. 4b), indicating that all the iodines are cleaved from the phenanthrene backbone. Therefore, the majority species of the isolated atoms trapped in the pores of the tessellation (green arrows in Fig. 3c) is identified as I adatoms. The minority species with the lower apparent height (yellow arrows in Fig. 3c) is associated with Ag adatoms trapped during formation of the tessellation, and no regular arrangement of majority and minority species was observed. In the C 1s XPS spectra, the low-binding-energy shoulder at ~ 283.5 eV becomes even more

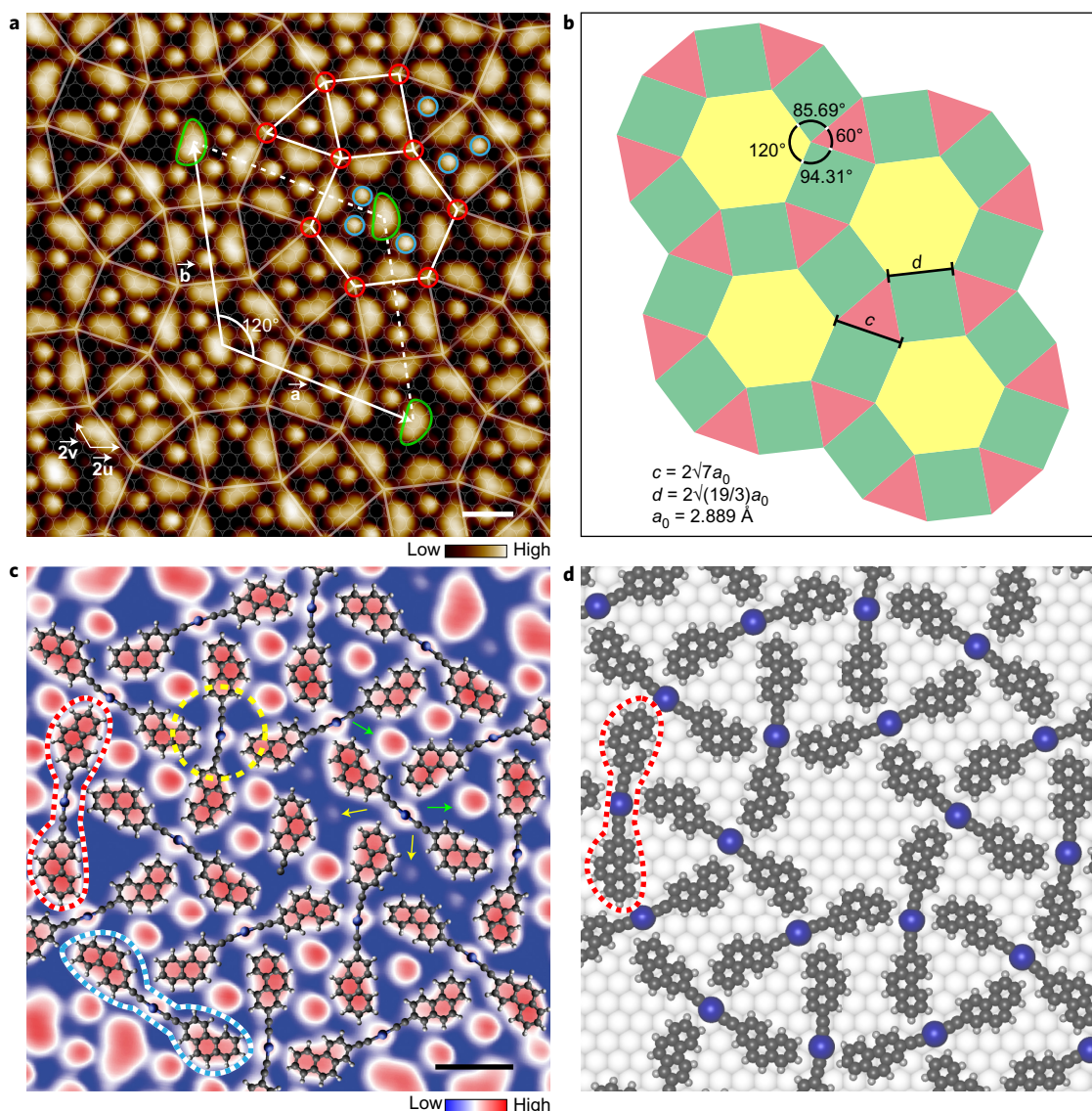


Figure 3 | AT (3.4.6.4) geometry and molecular-level expression. **a**, High-resolution STM image of (3.4.6.4) AT with a commensurate model as well as proposed registry superimposed. $I_t = 0.06$ nA, $U_b = -0.6$ V. Red circles highlight Ag complex nodes, blue circles highlight trapped adatoms, and green outlines highlight trapped single molecules. **b**, Tile representation of the (3.4.6.4) AT with geometric parameters. **c**, Magnified STM image of **a** superimposed with DFT-calculated chemical structures. The *cis* and *trans* conformers of BPE-Ag (**8**) are highlighted with dashed red and blue outlines, respectively. The yellow dashed circle highlights the bonding motif. Green and yellow arrows indicate trapped adatoms of different species. **d**, DFT-calculated (3.4.6.4) AT structure on Ag(111). The building block is highlighted with a red dashed outline. Ag, blue; C, grey; H, white. Scale bars: 10 Å.

prominent, contributing to 12% of the total area (blue and violet curves in Fig. 4a). As both carbons in the ethynyl group contribute to the shoulder feature⁴⁶, its relative area matches the expectation of 12.5% for an EP molecule (**3**) with its ethynyl group connected to a Ag atom. Thus the XPS data further corroborate the STM observation that nearly all the Ag-organic structures were converted to BPE-Ag (**8**) (Fig. 3c). A close-up STM image of the BPE-Ag building block (**8**) in the tessellation scheme shows that the hybrid Ag bridge becomes symmetric again, with both alkynyl-Ag connections appearing narrowed and the increased distance between two protrusions amounting to ~ 16 Å (Fig. 5f).

The chemical conversion of EIP tectons (**1**) is also evident in the near-edge X-ray absorption fine-structure (NEXAFS) spectra presented in Fig. 4c. The double-peak feature at ~ 285 eV corresponds to out-of-plane π^* resonances of the phenanthrene backbone⁵¹ and the ethynyl moiety, whereas the single peak at ~ 286 eV (dashed line in Fig. 4c) is related to the in-plane π^* resonance of the ethynyl group only⁴³. After two annealing steps, the dichroism of the out-of-plane

π^* resonances remains fully developed, indicating flat adsorption. The ethynyl peak is broadened and exhibits a weakened intensity. Together, these findings indicate a partial filling of the in-plane ethynyl π^* orbitals ascribed to hybridization with the Ag atom. These NEXAFS data are fully consistent with both STM and XPS observations.

Low-temperature C-H activation and convergent reaction. From the above discussion, there are two main characteristics involved in the reactions that lead to the formation of the (3.4.6.4) AT. The first notable feature is the C-H activation of the terminal alkynes, taking place at temperatures as low as 180 K, as observed by STM. The second feature is a 92% (for calculation see Supplementary Fig. 6) conversion of EIP (**1**) to BPE-Ag (**8**) after 300 K annealing, regardless of the diversity of the intermediate products appearing in a broad temperature range (180–250 K). In the following, based on the experimental observation and modelling insights, we formulated an exchange reaction scenario coherently explaining the two key features, along with other observations.

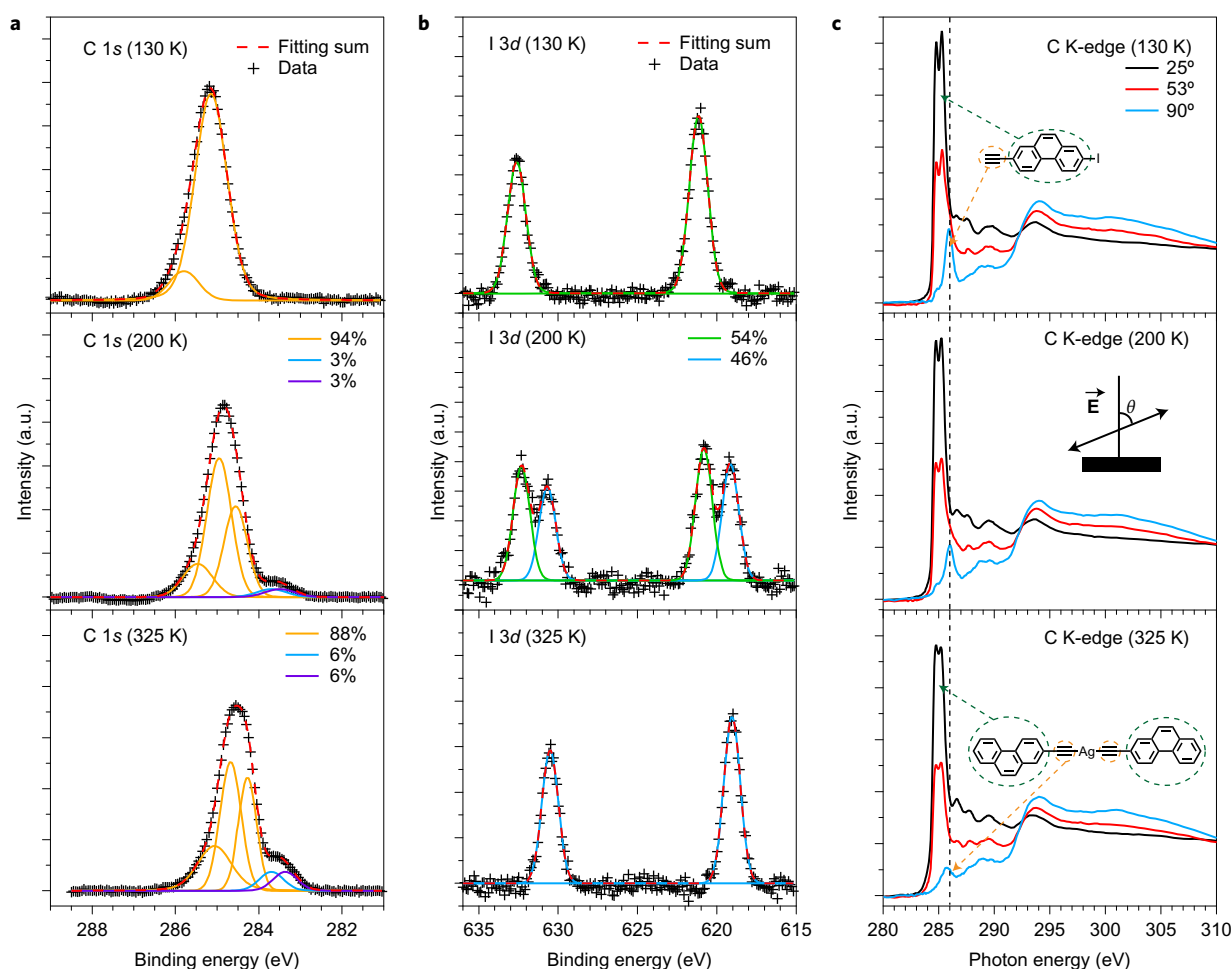


Figure 4 | XPS and NEXAFS characterization of chemical species occurring during the convergent reaction pathway. **a**, Carbon 1s XPS spectra of generated species on Ag(111) with EIP (**1**) subject to three annealing temperatures. Percentages correspond to relative contributions from different carbon species: blue and violet represent the two carbons in the ethynyl group bonded to Ag, whereas orange represents the remaining carbon species. **b**, Corresponding iodine 3d XPS signature. Percentages correspond to relative contributions from different iodine species: green, iodine covalently bonded to the phenanthrene backbone; blue, surface iodine adatoms. **c**, Angle-dependent carbon K-edge NEXAFS spectra of different EIP (**1**) phases on Ag(111) as a function of the photon angle of incidence (θ) at 25, 53 and 90°. Inset, middle: Angle θ with respect to electric field \mathbf{E} and surface normal. Dashed circles indicate the specific carbon atoms contributing dominantly to the peaks at different energies. For all panels, annealing temperatures (130, 200 or 325 K) are indicated top left. Data were obtained at a substrate temperature of 130 K.

After the onset of C–I dissociation above 130 K (Fig. 6, step i), several products coexist on the Ag(111) surface at 200 K, signalling an onset of the reaction (steps ii–iv, Fig. 6): intact EIP molecules (**1**, Fig. 5a); dehalogenated radical EP molecules (**2**, Fig. 5b); protonated EP molecules (**3**, Fig. 5c); aryl–Ag–aryl complexes (**4**, Fig. 5d); and alkynyl–Ag–aryl complexes (**6**, Fig. 5e). Annealing to 250 K is required to initiate the emergence of species featuring an alkynyl–Ag–alkynyl bridge (**8**, Fig. 5f and Supplementary Fig. 11). The aryl–Ag–aryl bridge in species **4** is reminiscent of the intermediates frequently encountered during on-surface Ullmann-type coupling reactions^{52,53}. Strikingly, **6** was observed at temperatures as low as 180–200 K, implying cleavage of the original alkynyl hydrogen through a previously unreported catalytic mechanism. Our previous DFT modelling has already recognized that the dehydrogenation barrier of terminal alkyne catalysed by a Ag adatom is even higher than directly by the Ag(111) substrate ($T_{\text{ann}} > 300 \text{ K}$)⁵⁴, which is consistent with earlier experimental results showing that terminal alkyne C–H activation is inhibited below room temperature^{46,55}.

The most probable catalyst for the C–H activation here is the hybrid Ag, that is, the Ag incorporated in the C–Ag–C bridge. Note that single Ag-terminated aryl–Ag or alkynyl–Ag were not observed, suggesting an energetic preference for the two-fold

bonding configuration. A detailed STM data analysis in conjunction with an earlier DFT examination⁴⁶ indicated a negatively charged hybrid-Ag bridge (Supplementary Figs 9 and 12). This could enable the attractive interaction between the hybrid Ag and the slightly positively charged H atom from the terminal alkyne. Here, we propose an exchange reaction mechanism as depicted in Fig. 6. After dehalogenation of EIP molecules (**1**) (step i), the radical site on the phenanthrene backbone could either bind to an atomic H on the surface, transforming into a protonated EP molecule (**3**) (step ii), or form an aryl–Ag–aryl bridge (step iii). A protonated EP molecule (**3**) can then approach the organometallic centre of **4** to form a putative species **5** by C–H activation (step iv). Transformation into species **6** continues by dehydrogenation of one of the aryl groups, forming **3** again, which detaches from **5**, leaving **6** behind (step v; see also Supplementary Movie 1). This exchange reaction pathway can be naturally reconciled with the coexistence of **3**, **4** and **6** at 200 K. Similar to **4**, the alkynyl–Ag–aryl bridge of **6** is also shown to be electron-rich on the surface (Supplementary Fig. 12). Moreover, the attractive interaction between **6** and **3** allows pre-organization in clusters (Fig. 5e and Supplementary Fig. 11), which favours the formation of putative species **7** during transformation from **6** to **8** based on a similar exchange process (step v; see also Supplementary Movie 2).

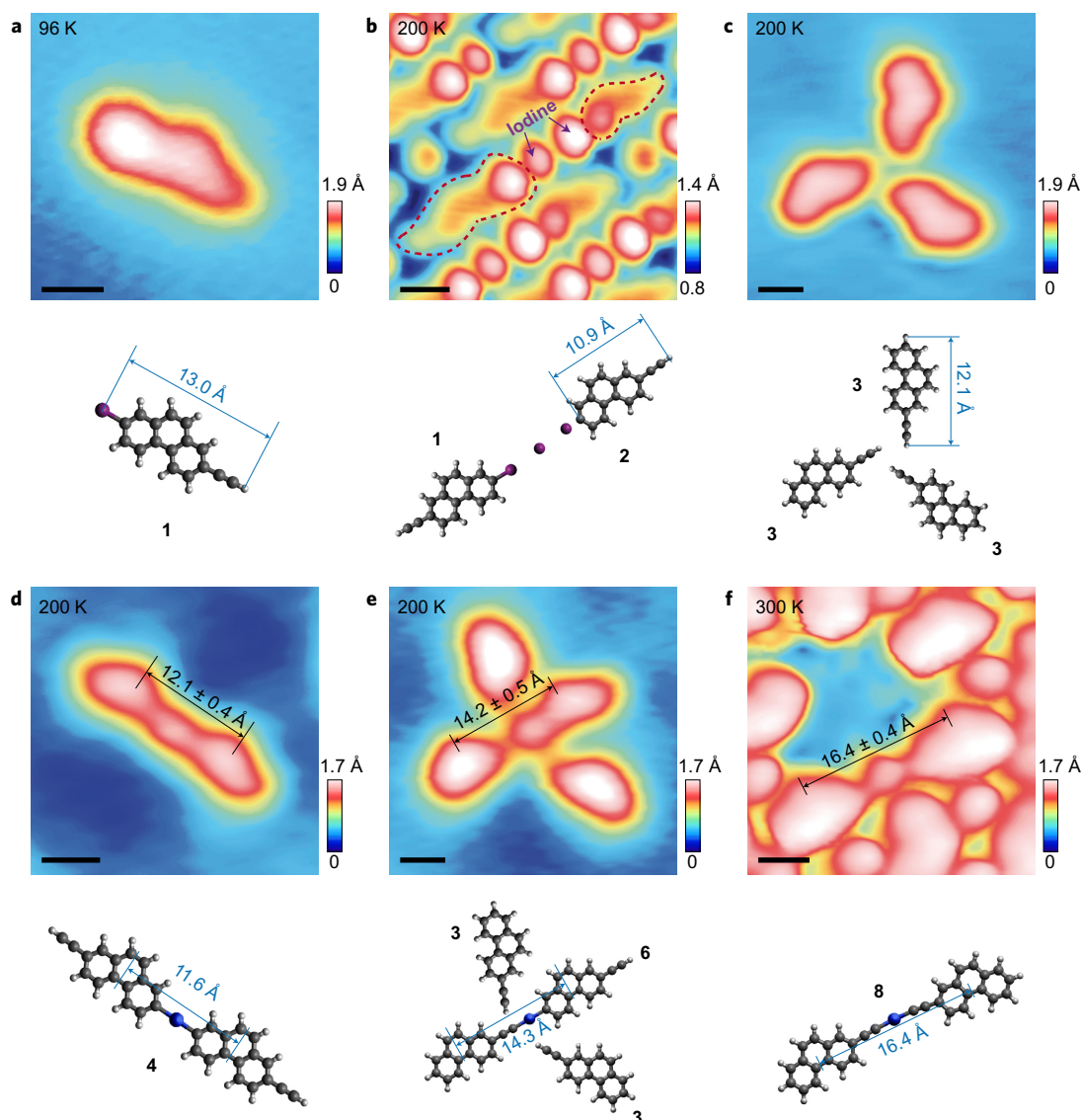


Figure 5 | Real-space characterization of temperature-dependent molecular species and cluster arrangements. STM images (upper panels) and DFT modelling (lower panels) of each species with characteristic lengths. **a**, Intact EIP molecule (**1**) isolated from the (6^3) network by molecular manipulation ($I_t = 0.1$ nA, $U_b = 0.05$ V). **b**, Dehalogenated radical EP molecules (**2**) ($I_t = 0.12$ nA, $U_b = -0.65$ V). **c**, A neutral EP molecular cluster (**3**) ($I_t = 0.03$ nA, $U_b = -0.05$ V). **d**, An aryl-Ag-aryl complex (**4**) ($I_t = 0.2$ nA, $U_b = -0.05$ V). **e**, An aryl-Ag-alkynyl complex (**6**) ($I_t = 0.2$ nA, $U_b = -0.05$ V). **f**, An alkynyl-Ag-alkynyl complex (**8**) ($I_t = 0.06$ nA, $U_b = -0.4$ V). The DFT calculated models are scaled to match the STM images. The red dashed outlines in **b** indicate an intact EIP (**1**) and a dehalogenated radical EP (**2**) molecule, respectively. The apparent height of the hybrid silver in **d-f** is scaled to 1 Å for comparison. Annealing temperatures are given in the STM images. Scale bars: 5 Å. The characteristic length for each Ag-complex shown in **d-f** is determined from averaging STM data obtained under similar experimental conditions (see Supplementary Fig. 10) with errors denoting standard deviations. Colour code for the structures: Ag, blue; I, purple; C, grey; H, white.

Note that both species **5** and **7** are elusive to STM observation, presumably due to their transient nature.

Alternative and simpler scenarios for C–H activation of terminal alkyne could be either a direct H transfer from the alkyne to the radical aryl site, or dehydrogenation by surface I adatoms. Such cases could also explain the formation of **6**, because Ag adatoms, radical alkynyls and radical aryls were all available on the surface. However, in both scenarios, products **4**, **6** and **8** should form immediately after C–H activation at 200 K. Consequently, the fact that species containing the alkynyl–Ag–alkynyl bridge were only observed after annealing at 250–300 K (Supplementary Fig. 11) rules out a direct C–H activation.

A basic requirement for the proposed pathway is that the dehalogenated site of the phenanthrene backbone must have undergone

hydrogenation. Several facts corroborate this assumption. From related situations⁴³ (Supplementary Fig. 8), a depression around the critical site would be expected if no hydrogenation had taken place. However, in high-resolution STM imaging, there is no hint of such a depression (Supplementary Figs 9 and 12). Next, a strong geometrical distortion towards the surface should follow from the significant interaction between the unsaturated backbone site and the surface⁴³. DFT modelling confirms that relevant distortion would appear for an unsaturated phenanthrene (Supplementary Fig. 13). Conversely, the NEXAFS data of the 325 K annealed sample exhibit a fully developed dichroism (Fig. 4c) of the phenanthrene-related π^* orbitals⁵¹ (the main double-peak feature around 285 eV), certifying an adsorption geometry coplanar to the surface, thus ruling out the existence of

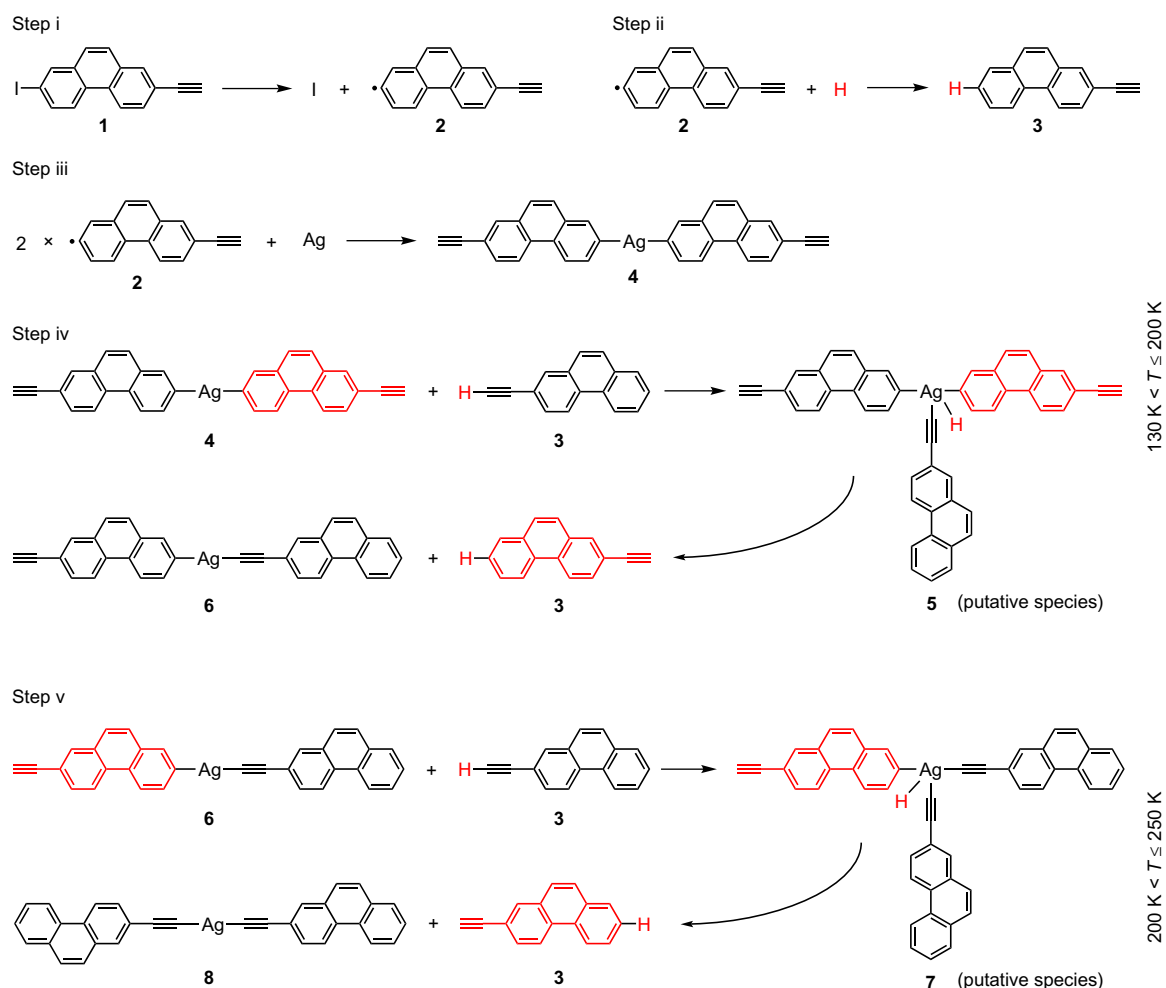


Figure 6 | Proposed convergent multi-step reaction pathway. In step i, the generated I radical is quickly quenched by surface electrons. All species are observed experimentally, except putative species **5** and **7**, for which the detailed bonding configuration is unknown. The H atom involved in transfer is highlighted in red, as is the exchanged EP (**3**) molecule in the organometallic complex. In steps i to iv, the reaction onset temperatures (T) are defined according to annealing temperatures employed for XS measurements. Step v sets in between 200 and 250 K.

unsaturated sites in **8**. Importantly, the proposed exchange reaction represents a mechanism enabling H transfer from the alkyne to the deiodinated aryl end without requiring the diffusion of H atoms over the surface. Therefore, conversion steps iv and v are not limited to temperatures below the onset of recombinative desorption of H from the Ag(111) surface (~ 180 K)^{49,50} and are thus plausible throughout the full temperature range required to explain the observations.

In this study, although the starting precursor is functionalized with both terminal alkyne and halogen groups, alkyne homocoupling⁴⁶, Ullmann-like coupling⁵³ as well as Sonogashira-like coupling⁵⁶ do not occur up to 350 K. A comparison with our previous investigation of alkyne precursors without halogen functionalities reveals an important aspect: the absence of conversion of the BPE-Ag (**8**) to a covalently linked dimer strongly corroborates the proposed homocoupling pathway⁵⁴ not involving organometallic intermediates on Ag(111).

To further cross-check that indeed the I abstraction enabling the generation of the catalytic Ag hybrid species is required for the proposed reaction pathway, we deposited EP (**3**) as the starting precursor on Ag(111) and examined its reactions in the same temperature range through combined STM and XS methods (Supplementary Figs 16 and 17). Because these experiments were carried out on the same Ag(111) surfaces, they exclude defects, step edges or varying amounts of isolated Ag adatoms as catalytic sites. No evidence of

hybrid Ag as well as (3.4.6.4) AT formation up to 325 K was found, providing consistent support for the above data interpretation.

Conclusions

We have demonstrated that a supramolecular expression of the semi-regular (3.4.6.4) AT can be achieved by interfacial chemical transformations of a simple, dissymmetric precursor on a smooth Ag(111) surface. The identified convergent multi-step reaction scenario leads to a network of high structural complexity exhibiting defect tolerance with respect to the embedding of by-products and integration of tecton conformers. Insights from complementary characterization techniques and computational modelling clearly evidence intermediate species and point to an intriguing exchange reaction, which allows for C–H activation and concomitant H transfer processes through a hybridized Ag species at temperatures as low as 180 K. Our approach opens up new avenues to construct complex materials through interfacial transformations of adsorbed molecular building blocks. Furthermore, our work may represent a case study for retracing surface-confined covalent engineering protocols in a retrosynthetic way based on the mechanistic insight obtained by the combination of scanning probe methods and spectroscopic techniques. This introduces novel opportunities to control covalent conversions by designing suitable starting materials, specifically when taking into account the particular laws of surface-confined reactions heavily diverging from solution chemistry. Finally, our

findings and methodology contribute to the general understanding of the emergence of complexity and hierarchic systems in chemistry and biology³⁶.

Methods

Chemicals. For details see Supplementary Information.

Sample preparation. Ag(111) metal surfaces were prepared *in situ* under UHV conditions by repeated cycles of Ar⁺ sputtering and annealing to 740–800 K. EIP (1) and EP (3) molecules were sublimated at crucible temperatures between 300 and 350 K onto cold substrates (~100 K), and annealing steps were performed afterwards.

STM experiments. The STM measurements were performed in two different set-ups: a commercial Joule-Thomson STM (JT-STM, SPECS) and a home-built Besocke-type STM, with base pressure better than 1×10^{-10} mbar in both set-ups. Data were recorded at equilibrium temperatures of 4.5 K (JT) and 5.5 K (Besocke) in two STMs. The unit cell parameters with proposed registry were obtained by averaging images of the same area with four different slow scanning directions to minimize error due to drift. The unit cell orientation with respect to the substrate could be determined by atomically resolving the Ag(111) at equilibrium temperatures.

XPS and NEXAFS experiments. The XPS and NEXAFS experiments were carried out at the HE-SGM monochromator dipole magnet beam light at the BESSY II synchrotron radiation source in Berlin, which provides light with a linear polarization of 90%. Photoelectrons were collected using a Scienta R3000 electron energy analyser. C 1s and I 3d spectra were acquired using excitation energies of 435 and 700 eV, respectively, in normal emission, and at a sample temperature of 130 K. The binding energy scale was calibrated against the Ag 3d_{5/2} line at 368.3 eV. For XPS spectra fitting, a Shirley (C 1s), or second-order polynomial background (I 3d) was subtracted from the raw data, and Voigt functions were used to fit the components.

For the NEXAFS measurements at the C K-edge, we used the partial electron yield mode of detection with a retarding voltage of 150 V. The NEXAFS spectra were acquired at a sample temperature of 130 K and referenced against a characteristic peak in simultaneously recorded spectra of a contaminated Au grid. Following a standard procedure, the signal of the bare crystal was subtracted from the raw data, and subsequently corrected for transmission through the beamline, normalizing the edge jump to 1.

Both XPS as well as NEXAFS data were recorded at a temperature of $T_{\text{meas}} = 130$ K, at which the (3.4.6.4) AT remains stable (Supplementary Fig. 18).

DFT calculations. DFT calculations with the surface were performed using the CP2K (<http://www.cp2k.org/>) package, in particular the QuickStep module⁵⁷. The computational parameters are similar to those used in a recent study⁵⁸. The Gaussian plane wave (GPW) method⁵⁹, where a cutoff of 750 Ry is used to expand the density and local potential in the plane-wave basis set and DZVP-MOLOPT basis set⁶⁰ to expand the orbitals, was used to solve the Kohn–Sham equations. The revised-B86-vdW-DF2 scheme⁶¹ was used to approximate the exchange–correlation term, with an explicitly non-local potential modelling the London dispersion forces. The effect of core electrons on the valence electrons was replaced by Goedecker–Teter–Hutter pseudo potentials⁶². Fractional occupation numbers were computed using the Fermi–Dirac distribution with the broadening corresponding to 500 K. Slab models were used to model the surface systems. Five layers of substrate were treated, of which the two bottom ones were kept fixed during structural relaxation. A lattice constant of 4.1074 Å was used, obtained by minimizing the energy of a bulk supercell. In total, 1,286 atoms and 12 molecules per unit cell were used for calculation. Despite using pseudo potentials, 11,722 electrons in doubly-occupied orbitals needed to be taken into account. This was possible because of the highly efficient implementation of the CP2K/QuickStep module and the use of the localized MOLOPT basis set.

Cluster DFT calculations were performed with the ORCA quantum chemistry code⁶³. The RPBE^{64,65} exchange–correlation functional was used. The structure was optimized with the def2-SVP basis set.

Data availability. Crystallographic data for the structure of compound 3', reported in the Supplementary Information, have been deposited at the Cambridge Crystallographic Data Centre under deposition no. CCDC 1515612. Copies of the data can be obtained free of charge at www.ccdc.cam.ac.uk/data_request/cif. The data that support the findings discussed here are available within the paper and its Supplementary Information, or from the corresponding authors upon reasonable request.

Received 16 October 2017; accepted 15 November 2017;
published online 22 January 2018

References

- Lehn, J.-M. *Supramolecular Chemistry: Concepts and Perspectives* (VCH, 1995).
- Moulton, B. & Zaworotko, M. J. From molecules to crystal engineering: supramolecular isomerism and polymorphism in network solids. *Chem. Rev.* **101**, 1629–1658 (2001).
- Kepler, J. *Harmonices Mundi* (Johannes Planck, 1619).
- Millan, J. A., Ortiz, D., van Anders, G. & Glotzer, S. C. Self-assembly of Archimedean tilings with enthalpically and entropically patchy polygons. *ACS Nano* **8**, 2918–2928 (2014).
- Shechtman, D., Blech, I., Gratias, D. & Cahn, J. W. Metallic phase with long-range orientational order and no translational symmetry. *Phys. Rev. Lett.* **53**, 1951–1953 (1984).
- Levine, D. & Steinhardt, P. J. Quasicrystals: a new class of ordered structures. *Phys. Rev. Lett.* **53**, 2477–2480 (1984).
- Ueda, K., Dotera, T. & Gemma, T. Photonic band structure calculations of two-dimensional Archimedean tiling patterns. *Phys. Rev. B* **75**, 195122 (2007).
- Basnarkov, L. & Urumov, V. Diffusion on Archimedean lattices. *Phys. Rev. E* **73**, 046116 (2006).
- Ramirez, A. P. Strongly geometrically frustrated magnets. *Annu. Rev. Mater. Sci.* **24**, 453–480 (1994).
- Tsai, A. P. & Yoshimura, M. Highly active quasicrystalline Al-Cu-Fe catalyst for steam reforming of methanol. *Appl. Catal. A* **214**, 237–241 (2001).
- Zhang, F., Liu, Y. & Yan, H. Complex Archimedean tiling self-assembled from DNA nanostructures. *J. Am. Chem. Soc.* **135**, 7458–7461 (2013).
- Zhang, F. *et al.* Self-assembly of complex DNA tessellations by using low-symmetry multi-arm DNA tiles. *Angew. Chem. Int. Ed.* **128**, 9006–9009 (2016).
- Tschierske, C. Liquid crystal engineering—new complex mesophase structures and their relations to polymer morphologies, nanoscale patterning and crystal engineering. *Chem. Soc. Rev.* **36**, 1930–1970 (2007).
- Talapin, D. V. *et al.* Quasicrystalline order in self-assembled binary nanoparticle superlattices. *Nature* **461**, 964–967 (2009).
- Asari, T., Arai, S., Takano, A. & Matsushita, Y. Archimedean tiling structures from ABA/CD block copolymer blends having intermolecular association with hydrogen bonding. *Macromolecules* **39**, 2232–2237 (2006).
- Hayashida, K., Dotera, T., Takano, A. & Matsushita, Y. Polymeric quasicrystal: mesoscopic quasicrystalline tiling in ABC star polymers. *Phys. Rev. Lett.* **98**, 195502 (2007).
- Barth, J. V., Costantini, G. & Kern, K. Engineering atomic and molecular nanostructures at surfaces. *Nature* **437**, 671–679 (2005).
- Elemans, J. A. A. W., Lei, S. B. & De Feyter, S. Molecular and supramolecular networks on surfaces: from two-dimensional crystal engineering to reactivity. *Angew. Chem. Int. Ed.* **48**, 7298–7332 (2009).
- Bartels, L. Tailoring molecular layers at metal surfaces. *Nat. Chem.* **2**, 87–95 (2010).
- Dong, L., Gao, Z. A. & Lin, N. Self-assembly of metal–organic coordination structures on surfaces. *Prog. Surf. Sci.* **91**, 101–135 (2016).
- Klappenberger, F. Two-dimensional functional molecular nanoarchitectures—complementary investigations with scanning tunneling microscopy and X-ray spectroscopy. *Prog. Surf. Sci.* **89**, 1–55 (2014).
- Tahara, K. *et al.* Two-dimensional porous molecular networks of dehydrobenzo [12]annulene derivatives via alkyl chain interdigitation. *J. Am. Chem. Soc.* **128**, 16613–16625 (2006).
- Schlickum, U. *et al.* Chiral Kagomé lattice from simple ditopic molecular bricks. *J. Am. Chem. Soc.* **130**, 11778–11782 (2008).
- Ecija, D. *et al.* Five-vertex Archimedean surface tessellation by lanthanide-directed molecular self-assembly. *Proc. Natl Acad. Sci. USA* **110**, 6678–6681 (2013).
- Shi, Z. L. & Lin, N. Porphyrin-based two-dimensional coordination Kagome lattice self-assembled on a Au(111) surface. *J. Am. Chem. Soc.* **131**, 5376–5377 (2009).
- Wasio, N. A. *et al.* Self-assembly of hydrogen-bonded two-dimensional quasicrystals. *Nature* **507**, 86–89 (2014).
- Urgel, J. I. *et al.* Quasicrystallinity expressed in two-dimensional coordination networks. *Nat. Chem.* **8**, 657–662 (2016).
- Glotzer, S. C. & Solomon, M. J. Anisotropy of building blocks and their assembly into complex structures. *Nat. Mater.* **6**, 557–562 (2007).
- Otero, R. *et al.* Elementary structural motifs in a random network of cytosine adsorbed on a gold(111) surface. *Science* **319**, 312–315 (2008).
- Marschall, M. *et al.* Random two-dimensional string networks based on divergent coordination assembly. *Nat. Chem.* **2**, 131–137 (2010).
- Newkome, G. R. *et al.* Nanoassembly of a fractal polymer: a molecular 'Sierpinski hexagonal gasket'. *Science* **312**, 1782–1785 (2006).
- Shang, J. *et al.* Assembling molecular Sierpinski triangle fractals. *Nat. Chem.* **7**, 389–393 (2015).
- Pivetta, M., Blüm, M.-C., Patthey, F. & Schneider, W.-D. Two-dimensional tiling by rubrene molecules self-assembled in supramolecular pentagons, hexagons, and heptagons on a Au(111) surface. *Angew. Chem. Int. Ed.* **47**, 1076–1079 (2008).
- Guillemet, O. *et al.* Self-assembly of fivefold-symmetric molecules on a threefold-symmetric surface. *Angew. Chem. Int. Ed.* **48**, 1970–1973 (2009).
- Bauert, T. *et al.* Building 2D crystals from 5-fold-symmetric molecules. *J. Am. Chem. Soc.* **131**, 3460–3461 (2009).
- Lehn, J.-M. Perspectives in chemistry—steps towards complex matter. *Angew. Chem. Int. Ed.* **52**, 2836–2850 (2013).

37. Nishio, M. CH/ π hydrogen bonds in crystals. *CrystEngComm* **6**, 130–158 (2004).
38. Bui, T. T. T., Dahaoui, S., Lecomte, C., Desiraju, G. R. & Espinosa, E. The nature of halogen–halogen interactions: a model derived from experimental charge-density analysis. *Angew. Chem. Int. Ed.* **48**, 3838–3841 (2009).
39. Cavallo, G. *et al.* The halogen bond. *Chem. Rev.* **116**, 2478–2601 (2016).
40. Brammer, L., Zhao, D., Ladipo, F. T. & Braddock-Wilking, J. Hydrogen bonds involving transition-metal centers—a brief review. *Acta Crystallogr. B* **51**, 632–640 (1995).
41. Braga, D., Grepioni, F. & Desiraju, G. R. Crystal engineering and organometallic architecture. *Chem. Rev.* **98**, 1375–1406 (1998).
42. Steiner, T. The hydrogen bond in the solid state. *Angew. Chem. Int. Ed.* **41**, 48–76 (2002).
43. Zhang, Y.-Q. *et al.* Unusual deprotonated alkynyl hydrogen bonding in metal-supported hydrocarbon assembly. *J. Phys. Chem. C* **119**, 9669–9679 (2015).
44. Raval, R. Chiral expression from molecular assemblies at metal surfaces: insights from surface science techniques. *Chem. Soc. Rev.* **38**, 707–721 (2009).
45. Zhou, X.-L. & White, J. M. Thermal decomposition of C₂H₅I on Ag(111). *Catal. Lett.* **2**, 375–384 (1989).
46. Zhang, Y.-Q. *et al.* Homo-coupling of terminal alkynes on a noble metal surface. *Nat. Commun.* **3**, 1286 (2012).
47. Di Giovannantonio, M. *et al.* Insight into organometallic intermediate and its evolution to covalent bonding in surface-confined Ullmann polymerization. *ACS Nano* **7**, 8190–8198 (2013).
48. Sun, Q. *et al.* Bottom-up synthesis of metalated carbyne. *J. Am. Chem. Soc.* **138**, 1106–1109 (2016).
49. Zhou, X.-L., White, J. M. & Koel, B. E. Chemisorption of atomic hydrogen on clean and Cl-covered Ag(111). *Surf. Sci.* **218**, 201–210 (1989).
50. Lee, G. & Plummer, E. W. Interaction of hydrogen with the Ag(111) surface. *Phys. Rev. B* **51**, 7250–7261 (1995).
51. Fronzoni, G. *et al.* Vibrationally resolved high-resolution NEXAFS and XPS spectra of phenanthrene and coronene. *J. Chem. Phys.* **141**, 044313 (2014).
52. Zhang, H. & Chi, L. Gold–organic hybrids: on-surface synthesis and perspectives. *Adv. Mater.* **28**, 10492–10498 (2016).
53. Lackinger, M. Surface-assisted Ullmann coupling. *Chem. Commun.* **53**, 7872–7885 (2017).
54. Björk, J., Zhang, Y.-Q., Klappenberger, F., Barth, J. V. & Stafström, S. Unraveling the mechanism of the covalent coupling between terminal alkynes on a noble metal. *J. Phys. Chem. C* **118**, 3181–3187 (2014).
55. Liu, J. *et al.* Lattice-directed formation of covalent and organometallic molecular wires by terminal alkynes on Ag surfaces. *ACS Nano* **9**, 6305–6314 (2015).
56. Kanuru, V. K. *et al.* Sonogashira coupling on an extended gold surface in vacuo: reaction of phenylacetylene with iodobenzene on Au(111). *J. Am. Chem. Soc.* **132**, 8081–8086 (2010).
57. VandeVondele, J. *et al.* Quickstep: fast and accurate density functional calculations using a mixed Gaussian and plane waves approach. *Comput. Phys. Commun.* **167**, 103–128 (2005).
58. Bacle, P., Seitsonen, A. P., Iannuzzi, M. & Hutter, J. Chemical reactions on metal-supported hexagonal boron nitride investigated with density functional theory. *Chimia* **68**, 596–601 (2014).
59. Lippert, G., Hutter, J. & Parrinello, M. A hybrid Gaussian and plane wave density functional scheme. *Mol. Phys.* **92**, 477–488 (1997).
60. VandeVondele, J. & Hutter, J. Gaussian basis sets for accurate calculations on molecular systems in gas and condensed phases. *J. Chem. Phys.* **127**, 114105 (2007).
61. Hamada, I. Van der Waals density functional made accurate. *Phys. Rev. B* **89**, 121103 (2014).
62. Goedecker, S., Teter, M. & Hutter, J. Separable dual-space Gaussian pseudopotentials. *Phys. Rev. B* **54**, 1703–1710 (1996).
63. Neese, F. The ORCA program system. *Wiley Interdiscip. Rev. Comput. Mol. Sci.* **2**, 73–78 (2012).
64. Hammer, B., Hansen, L. B. & Nørskov, J. K. Improved adsorption energetics within density-functional theory using revised Perdew–Burke–Ernzerhof functionals. *Phys. Rev. B* **59**, 7413–7421 (1999).
65. Perdew, J. P., Burke, K. & Ernzerhof, M. Generalized gradient approximation made simple. *Phys. Rev. Lett.* **77**, 3865–3868 (1996).

Acknowledgements

The authors acknowledge funding by the German Research Foundation (DFG) Excellence Cluster Munich Center for Advanced Photonics, DFG project KL 2294/3–1 and ERC Advanced Grant MolArt (no. 247299). M.R. acknowledges support by the DFG-priority programs 1459, TR88 ‘3Met’ and the KNMF facility (KIT, Germany). The authors thank the Helmholtz–Zentrum Berlin–Electron storage ring BESSY II for provision of synchrotron radiation at beamline HE-SGM and thank C. Wöll and A. Nefedov for providing access to the HE-SGM end station.

Author contributions

Y.-Q.Z., J.V.B. and F.K. conceived the experiments. Y.-Q.Z., L.Z. and T.L. performed the STM measurements and analysed the data. Y.-Q.Z., M.P., L.Z., T.L. and F.K. performed the spectroscopy experiments and analysed the data. A.P.S. carried out the DFT calculations. P.D., Z.C., S.K. and M.R. developed the synthesis of the molecules used. Y.-Q.Z., A.P.S., M.R., J.V.B. and F.K. co-wrote the paper. All authors discussed the results and commented on the manuscript.

Additional information

Supplementary information and chemical compound information are available in the [online version of the paper](#). Reprints and permissions information is available online at www.nature.com/reprints. Publisher’s note: Springer Nature remains neutral with regard to jurisdictional claims in published maps and institutional affiliations. Correspondence and requests for materials should be addressed to Y.-Q.Z., M.R., J.V.B. and F.K.

Competing financial interests

The authors declare no competing financial interests.